Research Article

Journal of
Environmental
Nanotechnology

Studies on Nd-doped Barium Cerate Nano-Sized Catalyst in Converting CH_4 into CO_2 at Lower Temperature

Khalid Ouzaouit[1], Abdelhay Aboulaich[2*]

[1]IM2NP Institute (UMR CNRS 7334), Sud Toulon-Var University, BP.132, 83957 La Grade, France

[2]Materials Science and Nano-Engineering Department, Mohammed VI Polytechnic University (UM6P), Lot 660, Hay Moulay Rachid, 43150 Benguerir, Morocco

Received: 03.08.2021 Accepted: 30.08.2021 Published: 30-09-2021

*Abdelhay.ABOULAICH@um6p.ma

ABSTRACT

The present paper describes the synthesis and first application of Nd-doped Barium cerate ($BaCeO_3$) nanoparticles as catalyst for the catalytic oxidation of methane (CH_4) into CO_2. Nd-doped $BaCeO_3$ nanoparticles, with the formula $BaNd_xCe_{(1-x)}O_3$, have been prepared using a simple sol gel method starting from acetate precursors. The as-prepared nanoparticles have been fully characterized by XRD, TEM, HRTEM and specific surface area measurements. Results confirmed the formation of highly crystallized nano-sized particles with small crystallite size. In-situ FTIR spectroscopy was used to study the catalytic conversion of methane (CH_4) into CO_2 in the presence of the as-prepared Nd-doped $BaCeO_3$ nanocatalyst. The catalytic properties of such nanocatalysts have been discussed and correlated to Nd-doping rate, crystallite diameter and specific surface area of the materials. Excellent catalytic properties have been obtained with $BaNd_{0.05}Ce_{0.95}O_3$, such as superior conversion efficiency, longer catalysis lifetime and lower activation temperature compared to un-doped $BaCeO_3$ catalyst. Interestingly, it was found that $BaNd_{0.05}Ce_{0.95}O_3$ nanocatalyst successfully converts the totality of CH_4 present in a mixture of CH_4-Air into CO_2 at a much lower temperature compared to the conventional Pd/Al_2O_3 catalyst.

Keywords: Oxidation of CH_4; Nd-doped $BaCeO_3$, Nanocatalysts, Noble metal-free catalysts, Sol-gel method, Greenhouse Gases (GHG).

1. INTRODUCTION

The threat of climate change to our planet is today greater than it has ever been. Global warming is one of the most serious effects of climate change. In both 2019 and 2020, the World Economic Forum (WEF) identified global warming and the failure of climate change adaptation and mitigation as one of the highest and most probable global risks for humanity. Global warming is in particular due to the increasing levels of greenhouse gases (GHGs), including carbon dioxide (CO_2), methane (CH_4) and nitrous oxide (N_2O), released in the atmosphere (Matthews *et al.* 2008). Such GHGs, which can last for years to centuries in the atmosphere, trap heat by absorbing solar radiation and cause the planet to get hotter. This alarming situation led to a global mobilization to achieve a deep reduction of GHG emission, which needs strong support from the scientific community. The reduction of fossil-based energy production, CO_2 emission from industrial plants, CO_2 capture and storage have been proposed and developed as a solution to climate change (Rishee Kumar Singh *et al.* 2020; Friedlingstein *et al.* 2020). Surprisingly, the capture of methane or its oxidation has not received the same attention as air capture of CO_2, while CH_4 is about 25 times more effective than CO_2 at trapping infrared radiation and causing global warming (Boucher *et al.* 2010). CH_4 is also the second most important anthropogenic GHG. Its atmospheric concentration is about 5 billion tonnes (Gt) vs 40 Gt of CO_2 in 2018. Recent reports stated that the oxidation of the 5 Gt of CH_4 currently available in the atmosphere would yield 8.2 Gt additional atmospheric CO_2, equivalent to a few months of current industrial CO_2 emission, but it would remove about 1/6 of total radiative forcing (Jackson *et al.* 2019). The reduction in short-term warming, attributable to the high radiative forcing of CH_4, could thus offer a complementary strategy to the removal of long-lived GHGs such as CO_2 and N_2O. The oxidation of CH_4 to CO_2 is a thermodynamically favorable reaction as shown by reaction 1.

$$CH_4 + O_2 \longrightarrow CO_2 + H_2O \qquad (1)$$

$$(\Delta H_{298} = -802.7 \text{ kj/mol})$$

However, as the C-H bond is highly stable, high activation energy is needed to split the methane's C-H bond and that is why methane conversion is usually operated at high temperature (600^{-1}-1100 °C) (Cui *et al.* 2018). In order to overcome this high activation energy,

https://dx.doi.org/10.13074/jent.2021.09.213439

catalytic oxidation of methane is used. The reaction is generally catalyzed by supported or unsupported metal oxide catalysts, such as Co_3O_4, Co_3O_4/Al_2O_3, $ZnCrO_4$, $CuCrO_4$, $PbCrO_4$, Cr_2O_3/Al_2O_3, CuO/Al_2O_3 and CeO_2/Al_2O_3, and noble metals based-catalysts such as Pd/Al_2O_3, Pt/Al_2O_3, Rh/Al_2O_3, Pt/SiO_2, Pd/SiO_2, etc. (Lee *et al.* 1995). Among the metal oxide catalysts, Co_3O_4 catalyst provided the highest activity, but its activity was much lower than Pd/alumina catalysts (Lee *et al.* 1995). Photocatalytic oxidation of CH_4, using ZnO, TiO_2 or metal-doped TiO_2 photocatalysts, has also been proposed in the literature (De_Richter *et al.* 2017). Perovskite-type oxide catalysts have also been studied for the catalytic oxidation of CH_4 (Arai *et al.* 1986). The highest active perovskite catalyst was $La_{0.6}Sr_{0.4}MnO_3$, which showed similar activity to Pt/Al_2O_3 catalyst at a conversion level below 80%. However, unlike the Pt/alumina catalyst, the catalytic activity with increasing temperature was significantly reduced at high conversion levels (Shimazaki *et al.* 2011). Even though, much progress has been made in decreasing the oxidation temperature of CH_4, most of the catalysts mentioned above still need temperature higher than 300 – 500 °C so that the CH_4 oxidation reaction can occur. Hence, the replacement of noble metal in CH_4 oxidation catalysts, while keeping high CH_4 conversion efficiency and low reaction temperature, remains a big challenge.

$BaCeO_3$-based ceramics and related compounds are very important materials because of their thermal and chemical stability and good ionic conduction properties, which allow these materials to be used in a wide range of applications, such as fuel cells, hydrogen separation membranes and hydrogen sensors (Yamanaka *et al.* 2003; Su *et al.* 2006; Bhowmick *et al.* 2010; Senthil Kumar *et al.* 2017; Madhuri Sailaja *et al.* 2017). Recently, some attempts have also been made to assess the catalytic properties of $BaCeO_3$ in the oxidative coupling of CH_4 and its conversion to C_2 products, like ethane and ethylene (Igenegbai *et al.* 2018).

In this study, the synthesis and the first application of Nd-doped $BaCeO_3$ nano-sized oxide in total conversion of CH_4 into CO_2 has been reported. The as-synthesized nanocatalyst showed very high conversion efficiency (up to 99.4 %) at much lower temperature compared to the conventional noble metal-based Pd/Al_2O_3 catalyst. The Nd doping rate of the as-prepared catalysts has been varied and correlated with nanocrystals diameter and specific surface area. The effect of all these parameters on the CH_4/CO_2 conversion efficiency in the presence of Nd-doped $BaCeO_3$ nanocatalysts has also been studied.

2. MATERIALS AND METHODS

2.1 Synthesis Method

In the first step, an appropriate amount of barium acetate (99.9 %), cerium acetate (99.9 %) and neodymium acetate (99.9%), supplied from Aldrich, corresponding to the theoretical formula of $BaNd_xCe_{(1-x)}O_3$, with x varied from 0 to 0.15, were dissolved in isopropanol. Then, the mixture was stirred for 1 hour until the total dissolution of the solid content in the solvent. The obtained solution was then heated at 80 °C under continuous stirring until formation of gel. The resulting gel was dried at 80 °C for 12 hours. Finally, the as-prepared powder was ground in an agate mortar and calcined at 950 °C for 5 hours with a heating and cooling rate of 5 °C/min. Pd/Al_2O_3 commercial catalyst containing 5% Pd (Sigma Aldrich) was used in this study for comparison.

2.2. Structural and Morphological Characterization

The XRD patterns were recorded using a Siemens – Brucker D5000 diffractometer. After a preliminary indexation using Winploter software, the lattice parameters were calculated and refined by least squares method (Roisnel *et al.* 2001). Crystallites sizes of the synthesized powders were estimated using Debye-Scherrer formula. Scanning electron microscopy (SEM) analyses were carried out using PHILIPS XL30 equipment in order to characterize the morphology of as-prepared catalysts. The thermal decomposition of the air-dried gel precursor of $BaNd_xCe_{(1-x)}O_3$ catalyst was investigated using differential thermal analysis (DTA) and thermogravimetric analysis (TGA), which have been carried out in the temperature range of 25 – 1100 °C with a TG-DTA 92 SETARAM equipment, with a heating rate of 5 °C/min. In order to characterize the porosity of the synthesized materials, nitrogen sorption isotherms were recorded at 77.35 K using a MICROMERITICS ASAP 2020 automatic apparatus, after an outgassing process of 12 hours at 90 °C under secondary vacuum. The specific surface area was determined by the Brunauer–Emmett–Teller (BET) method (Brunauer *et al.* 1938).

2.3. Experimental set-up for catalytic test

The experimental set-up used to measure the catalytic activity of the $BaNd_xCe_{(1-x)}O_3$ nanocatalysts, through the oxidation of CH_4 to CO_2, is schematized in the Fig.1. It includes three parts:

i) **Feed part** where the gas is supplied out using a bottle containing 2500 ppm of CH_4 diluted in air, one bottle containing pure oxygen (O_2) and the other one contains argon (Ar). The flowmeter is used to control the gas output. A mixer is used to prepare the gas mixture with desired composition. The catalytic oxidation of CH_4 was carried out with a fixed flow gas of 5 mL/minute.

ii) **Reactor part** which includes a quartz tube held in place with silica wool on both sides. The quartz tube containing the catalyst powder was oriented horizontally in a furnace and heated to the desired temperature at a rate of 2 K/min under argon flow.

iii) **Analysis part** or the analysis cell, where the outgoing gases are analyzed, is a quartz tube containing pellets of KBr at its two ends. The cell is placed in a FTIR spectrophotometer. The FTIR spectra were recorded between 400 cm^{-1} and 4000 cm^{-1}, with a resolution of 8 cm^{-1}.

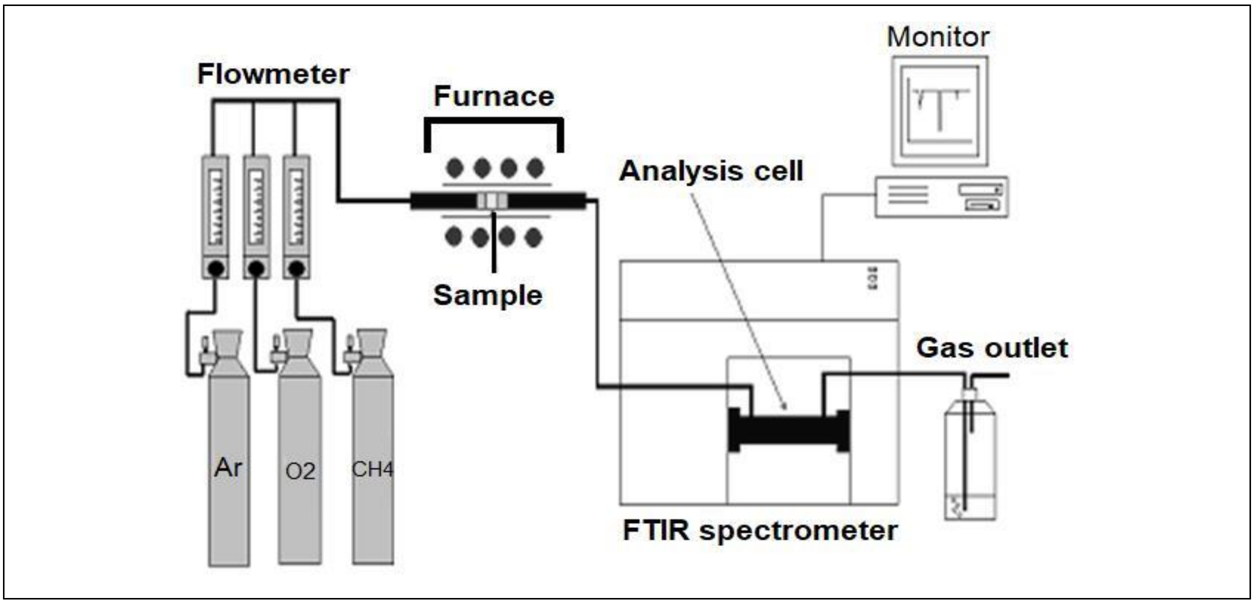

Fig. 1: The experimental set-up used in this study for the catalytic oxidation of CH_4 to CO_2

2.4. Catalytic activity measurement

In order to analyze the gas-solid reactivity over time and to evaluate the catalytic efficiency of our nanocatalysts at room and high temperature, in-situ FTIR measurements have been carried out according to the following procedure:

i) First of all, the catalytic cell is heated at the desired temperature, without any catalyst, in order to perform the blank experiment and control the purity of the cell itself; argon gas is injected in the cell with a flow gas of 5 mL/minute and a series of FTIR spectra are recorded.

ii) Then, in order to define a new blank experiment with catalyst only (without any active gas), the catalyst sample is introduced in the quartz tube, then argon flux is injected to evacuate room atmosphere (air with residual CO_2 and H_2O gases), FTIR spectra are also recorded in these conditions.

iii) Finally, in order to perform the catalytic test, the active gas (air with 2500 ppm of methane CH_4) is introduced at the desired temperature and simultaneously, a sequence of FTIR spectra is recorded at about 1-minute intervals.

The catalytic reaction is then monitored by the evolution of FTIR bands of CH_4 (characteristic bands at 3020 cm^{-1} and 1300 cm^{-1}), CO_2 (characteristic bands at 2350 cm^{-1} and 670 cm^{-1}) and H_2O (characteristic band at 1590 cm^{-1}), as shown in Fig. 2 (Supplementary Material). Assuming that the FTIR band intensity is proportional to the concentration of CH_4 and CO_2, the concentration of CH_4 and CO_2 at time ‘t’ can be calculated as below:

$$[CH_4]^* = I(CH_4)/I_{max}(CH_4)$$

with $I(CH_4)$ is the measured FTIR band surface of CH_4 and $I_{max}(CH_4)$ is the measured FTIR band surface of CH_4 in the absence of any catalytic interaction.

By the way, according to the reaction 1, when one mole of CH_4 is oxidized, one mole of CO_2 is formed. So, the concentration of CO_2 at time t can be calculated as below:

$$[CO_2]^* = 1 - [CH_4]^*$$

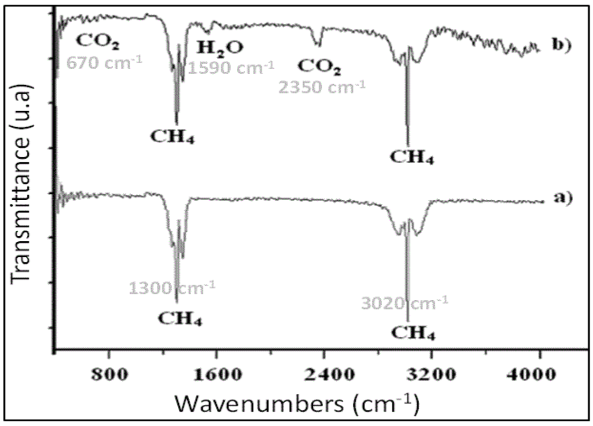

Fig. 2: Supplementary Material

Relative normalized values $[CH_4]^*$ and $[CO_2]^*$ are then used to represent the conversion rate of CH_4 into CO_2. For example, when $[CO_2]^*$ is equal to 1, this indicates a complete conversion of the 2500 ppm of CH_4 into 2500 ppm of CO_2. The CO_2 band at 2350 cm^{-1} was finally chosen to follow the catalytic reaction, because of its better definition in the spectra (Fig. 2, Supplementary Material).

3. RESULTS AND DISCUSSION

3.1 Preparation and characterization of nano-sized $BaNd_xCe_{(1-x)}O_3$ catalysts

Fig. 3 (Supplementary Material) shows the TGA and TDA results of dried gel precursor corresponding to the un-doped $BaCeO_3$ catalyst. The curves show a multi-step decomposition behavior, with an endothermic peak at 130 °C, related to the loss of moisture and dehydration of the precursors, an exothermic peak at around 325 °C, which can be attributed to the decomposition of the organic content of the gel. However, no weight loss was observed at temperature higher than 950 °C. The reactions involved in the synthesis of $BaCeO_3$ can be written as below:

- **For cerium precursor:**

$$Ce(CH_3COO)_3 + 3\,H_2O \rightarrow Ce(OH)_3 + 3\,CH_3COOH \tag{2}$$

$$2\,Ce(OH)_3 \rightarrow Ce_2O_3 + 3\,H_2O \tag{3}$$

$$Ce_2O_3 + \tfrac{1}{2}\,O_2 \rightarrow 2\,CeO_2 \tag{4}$$

- **For barium precursor:**

$$Ba(CH_3COO)_2 + 2\,H_2O \rightarrow Ba(OH)_2 + 2\,CH_3COOH \tag{5}$$

$$2\,Ba(OH)_2 \rightarrow 2\,BaO + 2\,H_2O \tag{6}$$

Therefore, the formation of barium cerate occurs according to:

$$BaO + CeO_2 \rightarrow BaCeO_3 \tag{7}$$

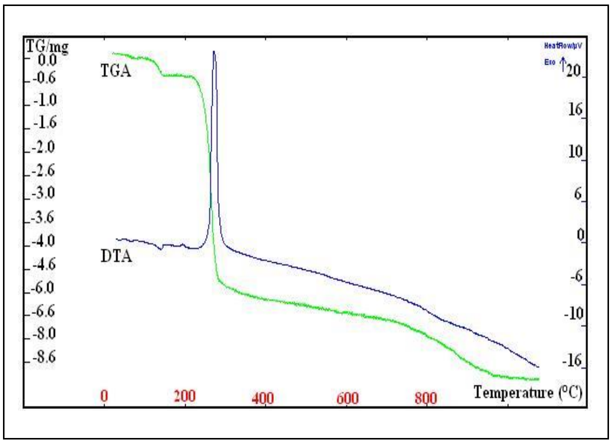

Fig. 3: Supplementary Material

The Fig. 4 shows the XRD pattern of $BaNdxCe_{(1-x)}O_3$ catalysts with different Nd content. The results showed that all the samples are well crystalized and all diffraction peaks of the samples are indexed as the orthorhombic perovskite structure, which matches with the JCPDS card number 22-0074.

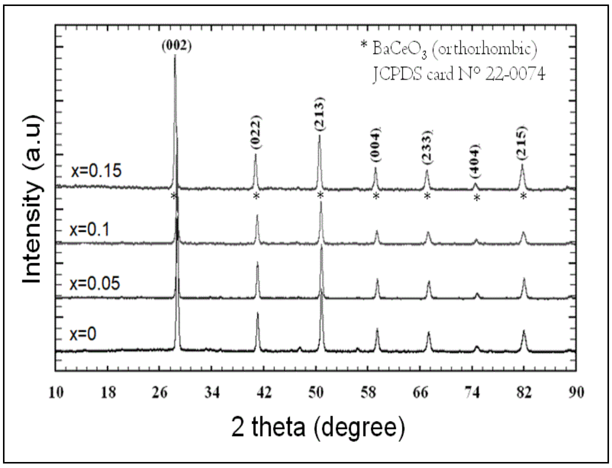

Fig. 4: XRD patterns of $BaNd_xCe_{(1-x)}O_3$ catalysts with x variation from 0 to 0.15%

The lattice parameters and average crystallite size of the samples have been calculated from XRD patterns and results are summarized in Table 1. The calculated lattice parameters are in good agreement with the values reported in the literature (Senthil Kumar *et al.* 2017). Results also showed that no significant change is observed in the lattice parameters with increasing Nd doping, indicating a homogeneous dispersion of Nd in the $BaCeO_3$ structure where Ce^{4+} sites would be substituted with Nd^{3+} ions. This substitution is facilitated by the very similar ionic radii between Ce^{4+} (1.11 Å) and Nd^{3+} (1.08 Å).

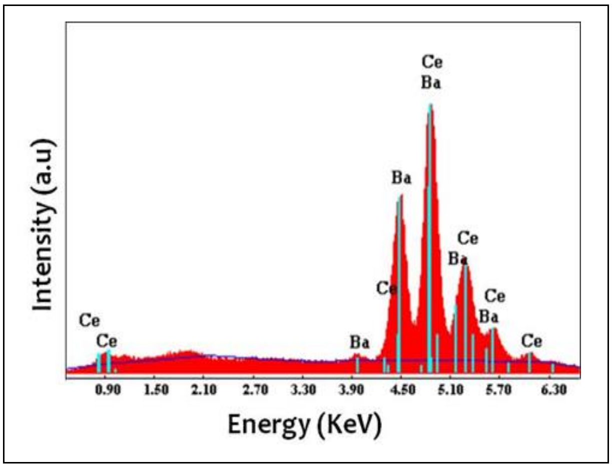

Fig. 5: Supplementary Material

Table 1: Lattice parameters and average crystallites size of $BaNd_xCe_{(1-x)}O_3$ nanocatalysts

Catalyst	a (Å)	b (Å)	c (Å)	Average crystallite diameter (nm)
$BaCeO_3$	8.776± 0.002	6.212 ± 0.004	6.231 ± 0.002	19.6 ± 0.5
$BaNd_{0.05}Ce_{0.95}O_3$	8.775 ± 0.003	6.210 ± 0.004	6.228 ± 0.005	18.4 ± 0.5
$BaNd_{0.1}Ce_{0.9}O_3$	8.771 ± 0.002	6.211 ± 0.004	6.229 ± 0.004	17.3 ± 0.5
$BaNd_{0.15}Ce_{0.85}O_3$	8.772 ± 0.002	6.210 ± 0.003	6.228 ± 0.004	17.0 ± 0.5

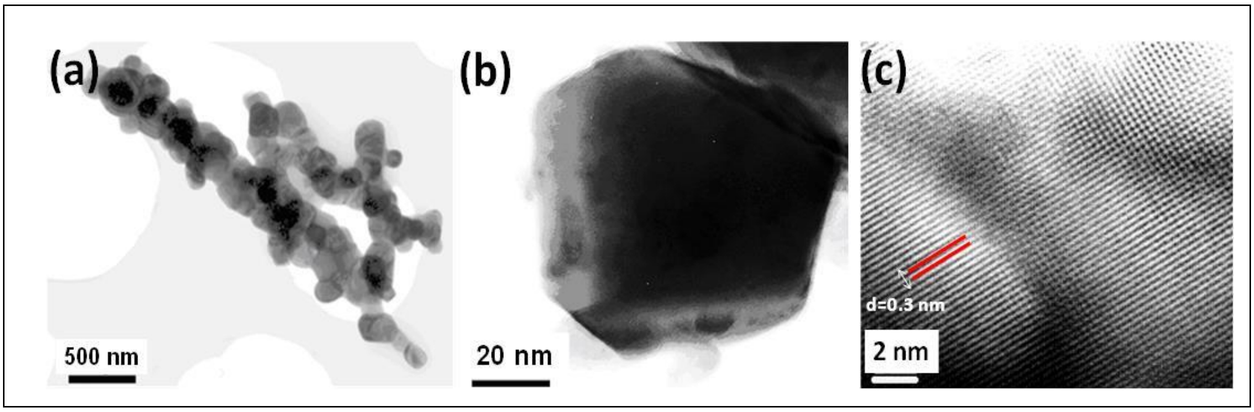

Fig. 6: TEM image (a) and HRTEM image (b-c) of $BaNd_{0.1}Ce_{0.9}O_3$ nanocatalyst

Moreover, results showed that crystallite diameter significantly decreases from about 20 nm to 17 nm when x is increased from 0 to 0.15. In addition to XRD results, the chemical composition of un-doped $BaCeO_3$ catalyst was confirmed by EDS measurement (Fig. 5, Supplementary Material).

The as-prepared nanocatalysts have also been observed by TEM. We should note that all the samples have similar morphology, which consists of agglomerates of nanocrystals of about 100 nm as shown in Fig. 6(a), in the case of $BaNd_{0.1}Ce_{0.9}O_3$. The formation of agglomerate of particles could result from the high surface/volume ratio of the nanocrystals. By the way, since the crystallite diameter calculated from XRD showed smaller nanocrystals, the particle size measured from TEM image suggests that particles are polycrystalline. HRTEM image also shows that the particles are highly crystalline with a lattice fringe spacing of d=0.3 nm (image 3(c)), which corresponds to the (002) plane of $BaCeO_3$ perovskite structure. Table 2 provides the specific surface area of the as-prepared $BaNd_xCe_{(1-x)}O_3$ catalysts calculated using BET method.

As can be seen from Table 2, all the samples exhibit a large surface area and thus are supposed to yield a high catalytic activity, since the heterogeneous catalytic reaction is generally enhanced by the high surface area of the catalyst. Results also showed that the surface area significantly increases with increasing Nd content, which is in agreement with the decrease of crystallite diameter with increasing Nd content, already shown in Table 1.

Table 2: BET surface area of $BaNd_xCe_{(1-x)}O_3$ nanocatalysts

Nanocatalyst	BET specific surface area (m^2g^{-1})
$BaCeO_3$	47.3
$BaNd_{0.05}Ce_{0.95}O_3$	53.7
$BaNd_{0.1}Ce_{0.9}O_3$	55.2
$BaNd_{0.15}Ce_{0.85}O_3$	56.5

3.2 Catalytic performance

3.2.1 Catalytic behavior of Nd-doped $BaCeO_3$ nanocatalysts

Fig. 7 shows the evolution of CH_4 conversion as a function of time at 300 °C in the presence of our $BaNd_xCe_{(1-x)}O_3$ nanocatalysts. The obtained curves are similar and present three characteristic parts:

i) the first one, which corresponds to a rapid increase in CO_2 absorbance, indicating an increase in the conversion rate of CH_4, can be associated with the active phase of the catalyst. This can be explained by the increasing adsorption of CH_4 on the active sites of the catalyst due to constant flow rate of CH_4, flowing through the catalytic material, which is also enhanced by the high surface area of the nanocatalysts.

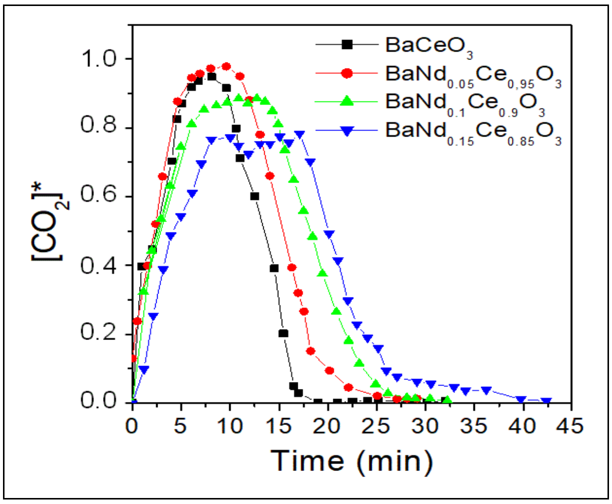

Fig. 7: Rate of catalytic conversion of CH_4 into CO_2 measured from FTIR spectroscopy (CO_2 vibrational band at 2350 cm^{-1} was used for monitoring the catalytic reaction)

ii) the second part, which corresponds to the top part of the curves where a maximum CO_2 formation is reached, results from the saturation of surface-active sites of the catalysts; this is because adsorbed methane molecules have reacted and the corresponding active sites have lost their reactivity.

iii) the third phase, which corresponds to the decrease in CH_4 conversion rate, can be ascribed to the damping of the catalysts. This is because the surface-active sites of the catalyst are no longer available to gas molecules and the catalytic reaction is stopped.

The catalyst lifetime of our $BaNd_xCe_{(1-x)}O_3$ nanocatalysts, which is defined as the time difference between the beginning of CH_4 conversion and the end of the saturation phase, can be estimated from the $[CO_2]^*$ vs. time curves (Fig. 7). This time increases from 19 to 40 minutes when the Nd content (x) is increased from 0 to 0.15 %, respectively, as shown in Table 3.

Table 3: Catalyst lifetime and CH_4 conversion rate of $BaNd_xCe_{(1-x)}O_3$ nanocatalysts

Nd Content (x %)	CH_4 conversion (%)	Catalyst lifetime (min)
0	95	19
0.05	98	25
0.1	88	28
0.15	78	40

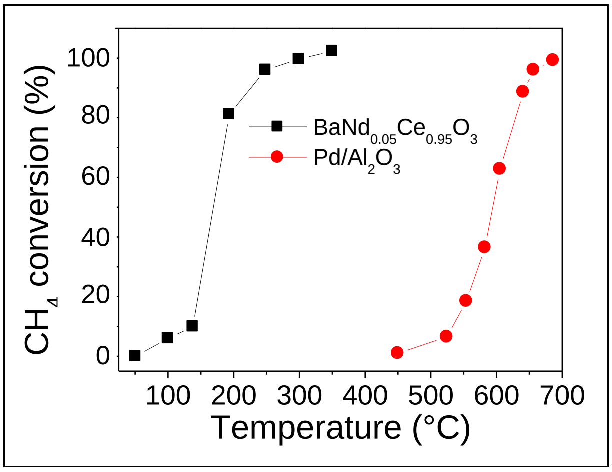

Fig. 8: The light-off curve of $BaNd_{0.05}Ce_{0.95}O_3$ nanocatalyst and Pd/Al_2O_3 commercial catalyst (CO_2 vibrational band at 2350 cm^{-1} was used to calculate the conversion rate)

Interestingly, results show that the barium cerate nanocatalyst doped with 5% Nd (compared to Ce content), with the formula $BaNd_{0.05}Ce_{0.95}O_3$, yields higher CH_4 conversion rate and improved catalysis lifetime compared to un-doped $BaCeO_3$ catalyst. The result is also in agreement with the surface area measurements (Table 2), which showed higher specific surface area for $BaNd_{0.05}Ce_{0.95}O_3$ compared to un-doped $BaCeO_3$ nanocatalyst. The 5% Nd-doped nanocatalyst was able to convert almost the totality of CH_4 into CO_2 with only about 8 minutes of reaction. The catalyst lifetime was also improved from 19 min (for un-doped catalyst) to 25 min. However, when the doping level exceeds 5% Nd, the conversion efficiency of CH_4 into CO_2 significantly decreases, even though the catalyst lifetime is remarkably enhanced, as shown in Table 3. These results indicate that the Nd content greatly affects the catalytic properties of $BaNd_xCe_{(`1-x)}O_3$ nanocatalyst and can thus be optimized to achieve the desired catalytic properties in terms of conversion efficiency and catalyst lifetime. The enhancement of the catalytic properties of 5% Nd-doped $BaCeO_3$ nanocatalyst compared to un-doped $BaCeO_3$ is likely due to higher production of oxygen vacancies when the Ce^{4+} sites are substituted by the trivalent Nd^{3+} dopant in the $BaCeO_3$ perovskite structure, which promotes the oxidation of CH_4 (Cheng *et al.* 2016). However, at doping rate higher than 5% Nd (compared to Ce), the quantity of oxygen vacancies produced by the nanocatalyst would be lower because of a significant partitioning of Nd dopant over both Ba and Ce sites, as already reported in the literature (Wu *et al.* 2005). Such partitioning reduces the concentration of oxygen vacancies, which, in turn, would lower the oxidizing ability of Nd-doped $BaCeO_3$ nanocatalyst. However, further investigations will be carried out for a deep understanding of the effect of Nd doping rate and the role of oxygen vacancies formation on CH_4 conversion efficiency of Nd-doped $BaCeO_3$ nanocatalyst.

3.2.2 Optimization of CH_4 conversion temperature

5% Nd-doped Barium cerate $BaNd_{0.05}Ce_{0.95}O_3$ nanocatalyst, which exhibited the highest CH_4 conversion efficiency was selected in order to optimize the conversion temperature of CH_4. A series of catalytic test was thus carried out at different temperatures in presence of $BaNd_{0.05}Ce_{0.95}O_3$ nanocatalyst. Fig. 8 shows the light-off curve of this material in comparison with the one obtained with Pd/Al_2O_3 commercial catalyst.

Results show that CH_4 conversion efficiency rapidly increases up to a temperature of about 250 °C where conversion rate is almost total. At higher temperatures, the conversion rate remains stable. Interestingly, more than 80 % CH_4 conversion is achieved at temperature as low as 200 °C, which indicates that Nd-doped $BaCeO_3$ nanocatalyst needs much lower activation temperature compared to noble metal-based catalysts that generally require temperature higher than 500 °C to be active, as shown by Fig. 8.

4. CONCLUSION

Nd-doped $BaCeO_3$ nanocatalysts, with different Nd doping rate, have been successfully synthesized using a simple sol-gel method starting from acetate precursors in isopropanol solvent. The as-prepared materials have been fully characterized with different characterization methods which confirmed the formation of highly crystallized nano-sized spherical particles with crystallite diameter of 17-20 nm, depending on Nd doping rate. The catalytic performances of the as-prepared nanocatalysts have also been measured through the catalytic conversion of CH_4 into CO_2 at different temperatures. To the best of our knowledge, this is the first application of such nanomaterials for total catalytic conversion of CH_4 into CO_2. The 5% Nd-doped $BaCeO_3$ nanocatalyst shows the highest CH_4 conversion rate (98%) and improved catalyst lifetime (25 min.) compared to un-doped $BaCeO_3$ nanocatalyst (95% and 19 min., respectively). Moreover, the light-off curve of 5% Nd-doped $BaCeO_3$ nanocatalyst showed that the catalyst has much lower activation temperature compared to noble metal-based Pd/Al_2O_3 catalysts. Finally, these results substantiate the great potential of Nd-doped $BaCeO_3$ nanocatalyst to be applied as an alternative material to noble metal-based catalyst, for the catalytic oxidation of CH_4 into CO_2. The application of such nanocatalysts for the catalytic conversion of CH_4 into syngas and value-added products will also be explored in the near future.

ACKNOWLEDGMENT

We thank both M. J. L Gonzales (IFREMER, Toulon) for helping us during BET measurements and M. M. ISA (L2MP Toulon) for his participation in the FTIR catalytic measurements.

SUPPLEMENTARY MATERIAL

This section includes the Fig. 2: FTIR spectra of active gas (2500 ppm CH_4 in air) recorded before (a) and after (b) 1 minute passing through the catalyst, S2: DTA and TGA curves of the dried precursor gel corresponding to $BaNd_{0.05}Ce_{0.95}O_3$ product. S3: EDS spectrum of un-doped $BaCeO_3$ nanocatalyst.

FUNDING

This research received no specific grant from any funding agency in the public, commercial, or not-for-profit sectors.

CONFLICTS OF INTEREST

The authors declare that there is no conflict of interest.

COPYRIGHT

REFERENCES

Arai, H., Yamada, T., Eguchi, K. and Seiyama, T., Catalytic combustion of methane over various perovskite-type oxides, *Appl. Catal.*, 26, 265–276 (1986). https://dx.doi.org/10.1016/S0166-9834(00)82556-7

Bhowmick, S., Basu, J., Xue, Y. and Carter, C. B., Hydrothermal synthesis of nanocrystalline barium cerate using hexamethylenetetramine, *J. Am. Ceram. Soc.*, 93(12), 4041–4046 (2010). https://dx.doi.org/10.1111/j.1551-2916.2010.03998.x

Boucher, O. and Folberth, G. A., New Directions: Atmospheric methane removal as a way to mitigate climate change?, *Atmos. Environ.*, 44(27), 3343–3345 (2010). https://dx.doi.org/10.1016/j.atmosenv.2010.04.032

Brunauer, S., Emmett, P. H. and Teller, E., Adsorption of gases in multimolecular layers, *J. Am. Chem. Soc.*, 60(2), 309–319 (1938). https://dx.doi.org/10.1021/ja01269a023

Cheng, Z., Qin, L., Guo, M., Xu, M., Fan, J. A. and Fan, L.-S., Oxygen vacancy promoted methane partial oxidation over iron oxide oxygen carriers in the chemical looping process, *Phys. Chem. Chem. Phys.*, 18(47), 32418–32428 (2016). https://dx.doi.org/10.1039/C6CP06264D

Cui, X., Li, H., Wang, Y., Hu, Y., Hua, L., Li, H., Han, X., Liu, Q., Yang, F., He, L., Chen, X., Li, Q., Xiao, J., Deng, D. and Bao, X., Room-temperature methane conversion by graphene-confined single iron atoms, *Chem.*, 4(8), 1902–1910 (2018).
https://dx.doi.org/10.1016/j.chempr.2018.05.006

de_Richter, R., Ming, T., Davies, P., Liu, W. and Caillol, S., Removal of non-CO_2 greenhouse gases by large-scale atmospheric solar photocatalysis, *Prog. Energy Combust. Sci.*, 60, 68–96 (2017).
https://dx.doi.org/10.1016/j.pecs.2017.01.001

Friedlingstein, P., O'Sullivan, M., Jones, M. W., Andrew, R. M., Hauck, J., Olsen, A., Peters, G. P., Peters, W., Pongratz, J., Sitch, S., Le Quéré, C., Canadell, J. G., Ciais, P., Jackson, R. B., Alin, S., Aragão, L. E. O. C., Arneth, A., Arora, V., Bates, N. R., Becker, M., Benoit-Cattin, A., Bittig, H. C., Bopp, L., Bultan, S., Chandra, N., Chevallier, F., Chini, L. P., Evans, W., Florentie, L., Forster, P. M., Gasser, T., Gehlen, M., Gilfillan, D., Gkritzalis, T., Gregor, L., Gruber, N., Harris, I., Hartung, K., Haverd, V., Houghton, R. A., Ilyina, T., Jain, A. K., Joetzjer, E., Kadono, K., Kato, E., Kitidis, V., Korsbakken, J. I., Landschützer, P., Lefèvre, N., Lenton, A., Lienert, S., Liu, Z., Lombardozzi, D., Marland, G., Metzl, N., Munro, D. R., Nabel, J. E. M. S., Nakaoka, S.-I., Niwa, Y., O'Brien, K., Ono, T., Palmer, P. I., Pierrot, D., Poulter, B., Resplandy, L., Robertson, E., Rödenbeck, C., Schwinger, J., Séférian, R., Skjelvan, I., Smith, A. J. P., Sutton, A. J., Tanhua, T., Tans, P. P., Tian, H., Tilbrook, B., van der Werf, G., Vuichard, N., Walker, A. P., Wanninkhof, R., Watson, A. J., Willis, D., Wiltshire, A. J., Yuan, W., Yue, X. and Zaehle, S., Global carbon budget 2020, *Earth Syst. Sci. Data.*, 12(4), 3269–3340 (2020).
https://dx.doi.org/10.5194/essd-12-3269-2020

Igenegbai, V. O., Meyer, R. J. and Linic, S., In search of membrane-catalyst materials for oxidative coupling of methane: Performance and phase stability studies of gadolinium-doped barium cerate and the impact of Zr doping, *Appl. Catal. B Environ.*, 230, 29–35 (2018).
https://dx.doi.org/10.1016/j.apcatb.2018.02.040

Jackson, R. B., Solomon, E. I., Canadell, J. G., Cargnello, M. and Field, C. B., Methane removal and atmospheric restoration, *Nat. Sustain.*, 2(6), 436–438 (2019).
https://dx.doi.org/10.1038/s41893-019-0299-x

Lee, J. H. and Trimm, D. L., Catalytic combustion of methane, *Fuel Process. Technol.*, 42(2–3), 339–359 (1995).
https://dx.doi.org/10.1016/0378-3820(94)00091-7

Madhuri Sailaja, J., Vijaya Babu, K., Murali, N. and Veeraiah, V., Effect of strontium on Nd doped $Ba_{1-x}Sr_xCe_{0.65}Zr_{0.25}Nd_{0.1}O_{3-\delta}$ proton conductor as an electrolyte for solid oxide fuel cells, *J. Adv. Res.*, 8(3), 169–181 (2017).
https://dx.doi.org/10.1016/j.jare.2016.12.006

Matthews, H. D. and Caldeira, K., Stabilizing climate requires near-zero emissions, *Geophys. Res. Lett.*, 35(4), L04705 (2008).
https://dx.doi.org/10.1029/2007GL032388

Rishee Kumar Singh, Vikas Srivastava, Atul, Ashhad Imam, Mehta, An endeavour to decrease CO_2 outflow through efficient use of supplementary cementitious materials in construction, *J. Environ. Nanotechnol.*, 9(3), 30–33 (2020).
https://dx.doi.org/10.13074/jent.2020.09.203420

Roisnel, T. and Rodriguez-Carvajal, WinPLOTR: A Windows tool for powder diffraction patterns analysis, *Mater. Sci. Forum.*, (378-381), 118–123 (2001).
https://dx.doi.org/10.4028/www.scientific.net/MSF.378-381.118

Senthil Kumar, A., Balaji, R., Puviarasu, P. and Jayakumar, S., Structural and morphological analysis of barium cerate electrolyte for SOFC application, *Mater. Sci.*, 35(1), 120–125 (2017).
https://dx.doi.org/10.1515/msp-2017-0021

Shimazaki, Y., Arai, N., Dunn, T. J., Yajima, T., Tani, F., Ramogida, C. F. and Storr, T., Influence of the chelate effect on the electronic structure of one-electron oxidized group 10 metal(ii)-(disalicylidene)diamine complexes, *Dalt. Trans.*, 40(11), 2469-2479 (2011).
https://dx.doi.org/10.1039/c0dt01574a

Su, X., Yan, Q., Ma, X., Zhang, W., Ge, C., Effect of co-dopant addition on the properties of yttrium and neodymium doped barium cerate electrolyte, *Solid State Ionics.*, 177(11–12), 1041–1045 (2006).
https://dx.doi.org/10.1016/j.ssi.2006.02.047

Wu, J., Davies, R. A., Islam, M. S. and Haile, S. M., Atomistic study of doped $BaCeO_3$: Dopant site-selectivity and cation nonstoichiometry, *Chem. Mater.*, 17(4), 846–851 (2005).
https://dx.doi.org/10.1021/cm048763z

Yamanaka, S., Fujikane, M., Hamaguchi, T., Muta, H., Oyama, T., Matsuda, T., Kobayashi, S. and Kurosaki, K., Thermophysical properties of $BaZrO_3$ and $BaCeO_3$, *J. Alloys Compd.*, 359(1–2), 109–113 (2003).
https://dx.doi.org/10.1016/S0925-8388(03)00214-7